Bioactive Materials 5 (2020) 201–209

Contents lists available at ScienceDirect

Bioactive Materials

journal homepage: http://www.keaipublishing.com/biomat

Ce and Er Co-doped TiO_2 for rapid bacteria- killing using visible light

Yawei Ren[a], Yajing Han[a,**], Zhaoyang Li[a], Xiangmei Liu[b,***], Shengli Zhu[a], Yanqin Liang[a], Kelvin Wai Kwok Yeung[c], Shuilin Wu[a,*]

[a] The Key Laboratory of Advanced Ceramics and Machining Technology by the Ministry of Education of China, School of Materials Science & Engineering, Tianjin University, Tianjin, 300072, China

[b] Ministry-of-Education Key Laboratory for the Green Preparation and Application of Functional Materials, Hubei Key Laboratory of Polymer Materials, School of Materials Science & Engineering, Hubei University, Wuhan, 430062, China

[c] Department of Orthopaedics & Traumatology, Li Ka Shing Faculty of Medicine, The University of Hong Kong, Pokfulam, Hong Kong, 999077, China

ARTICLE INFO

Keywords:
Photocatalytic
TiO_2
Antibacterial
Doping
Light responsive

ABSTRACT

Bacterial infection and related diseases are threatening the health of human beings. Photocatalytic disinfection as a simple and low-cost disinfection strategy is attracting more and more attention. In this work, TiO_2 nanoparticles (NPs) were modified by co-doping of Ce and Er using the sol–gel method, which endowed TiO_2 NPs with enhanced visible light photocatalytic performance but not pure ultraviolet photocatalytic properties compared the untreated TiO_2. Our results disclosed that as the doping content of Er increased, the photocatalytic activity of modified TiO_2 NPs initially increased and subsequently decreased. The same trend occurred for Ce doping. When the doping dose of Er and Ce is 0.5 mol% and 0.2 mol%, the 0.5Ce0.2Ti–O calcined at 800 °C presented the best antibacterial properties, with the antibacterial efficiency of 91.23% and 92.8% for *Staphylococcus aureus* and *Escherichia coli*, respectively. The existence of Er ions is thought to successfully turn the near-infrared radiation into visible region, which is easier to be absorbed by TiO_2 NPs. Meanwhile, the addition of Ce ions can effectively extend spectral response range and inhibit the recombination of electrons and holes, enhancing the photocatalytic disinfection activity of co-doped TiO_2.

1. Introduction

Bacteria can cause enormous health problems for human beings. Some reports have revealed that bacterial infections and related complications are the second leading cause of death, affecting 15 million people approximately each year [1–3]. As s we all known, since the invention of penicillin by Alexandar Fleming, antibiotics were widely utilized to cope with diseases caused by bacteria. Nevertheless, the misuse and overuse of traditional antibiotics have already led to the appearance of bacterial resistance and even the occurrence of multi-drug-resistant (MDR) bacteria of “superbugs” [4]. A recent study predicts that superbugs may cause the death of over 10 million people by 2050 [5,6]. On this basis, the development of antibiotics-free disinfection strategy is urgently needed [7,8]. Among these strategies, visible light disinfection can effectively kill bacteria as a nonresistant and minimally invasive process [9,10]. Compared with antibiotics, it can destroy physiological activities of bacteria in a shorter time through the radical oxygen species (ROS), such as $\cdot O_2^-$, ·OH, $^1O_2$ and H_2O_2, which are produced by photocatalysts [11–13]. Among various photocatalysts, TiO_2 is the most common one thanks to its low toxicity and long-term photostability. However, TiO_2 possesses a wide band gap of 3.0, 3.13, and 3.2 eV for rutile, brookite and anatase, respectively, which makes it can only be driven by ultraviolet (UV) light [14–16]. Long time irradiation under strong UV light is harmful for health. In addition, UV only accounts for less than 5% of the whole sunlight. Hence, much effort has been made to modify TiO_2 NPs to broaden light absorbance, including element doping, noble metal deposition, heterojunction construction, and so on [15,17–20]. Recently, Guayaquil-Sosa et al. synthesized Pt on mesoporous TiO_2 using a non-thermal assisted sol-gel and reduced the band gap to 2.34 eV [21]. Zhu et al. prepared a new class of red phosphorus (RP) decorated TiO_2 and largely extended the optical light harvesting ability [22]. The rapid recombination of photogenerated electron-hole pairs is another problem which limits the photocatalytic property of TiO_2. Up to now, Ce doping

Peer review under responsibility of KeAi Communications Co., Ltd.
* Corresponding author.
** Corresponding author.
*** Corresponding author.
E-mail addresses: hanyajing@tju.edu.cn (Y. Han), liuxiangmei1978@163.com (X. Liu), shuilinwu@tju.edu.cn (S. Wu).

https://doi.org/10.1016/j.bioactmat.2020.02.005
Received 27 December 2019; Received in revised form 3 February 2020; Accepted 4 February 2020

has been extensively studied and proved to be effective on reducing the band gap and suppressing the recombination of electron–holes, thanks to its incompletely occupied 4f and 5d electron orbitals [23,24]. Er-doping have received considerable attention for frequency up-conversion of infrared radiation into visible light with the suitable host matrix and ion concentration [25–27]. However, few studies have reported the dual elemental doping for TiO_2 NPs.

In this work, TiO_2 photocatalysts with different dopant contents of Ce and Er were synthesized using a sol–gel process. Furthermore, their photocatalytic properties were investigated through the degradation of methyl orange (MO) and their antibacterial performances were assessed by spread plate using *E. coli* and *S. aureus*.

2. Experimental

2.1. Materials preparation

Anhydrous ethanol, glacial acetic acid, titanium butoxide (Ti(O$(C_4H_9))_4$), cerium nitrate hexahydrate, erbium nitrate pentahydrate and polyethylene glycol (PEG 400) were all purchased from Aladdin Shanghai. Deionized water (DI) was used for washing. And all the chemicals were used as received without any purification.

Pure TiO_2, a series of Er doped TiO_2 and Er–Ce co-doped TiO_2 photocatalysts were synthesized by sol–gel method [28–30]. The preparation process was schematically diagrammatized in Scheme 1. Briefly, 10 ml of titanium butoxide (Ti(O$(C_4H_9))_4$) was added into 20 ml of anhydrous ethanol and 5 ml of glacial acetic acid with for 30 min stirring to form solution A. In the preparation process of mono-doped and co-doped TiO_2 NPs, calculated amounts of cerium nitrate hexahydrate and erbium nitrate pentahydrate were added into solution A. 10 ml of absolute ethanol, 1.8 ml of DI and 1 ml of PEG 400 were mixed to get solution B. In the followed step, solution B was dropped into solution A with constant stirring condition to obtain homogeneous sol. The final solution was heated up to 60 °C and reacted for 2 h to transform into gel. The gel was then aged at room temperature for a day and dried at 80 °C in vacuum. Subsequently, the samples were washed to remove residual chemicals, dried in a vacuum and annealed for 3 h.

2.2. Characterization

Scanning electron microscope (SEM, Hitachi S-4800, Japan) analysis equipped with an energy dispersive X-ray spectroscopy (EDS, Oxford X-max20, UK) and transmission electron microscope (TEM, JEM-2100F, Japan) were used to characterize the sample morphologies. X-ray diffractometer (XRD, D8 Advanced, Germany) was used to identify the crystal structure of TiO_2 with Cu-kα radiation (λ = 1.5406 Å), operated with the step size of 2°/min in the range of 2θ = 20–80°. The Raman spectra were obtained to prove the presence of surface defects using a Raman microscope (DXR2, Thermo Scientific, USA) under 532 nm laser excitation. X-ray photoelectron spectroscopy (XPS) analysis was utilized to determine the surface chemical species of the particles (ESCALAB 250Xi, Thermo Scientific, USA). The diffuse reflectance ultraviolet–visible (DR UV–vis, UV-2700, Japan)) spectrum was carried out to achieve the absorption spectra of photocatalysts in the range of 200–800 nm with $BaSO_4$ as a reference. The band energy gap can be calculated using the following formula [17]:

$$(Ah\nu)^{1/2} = C\,(h\nu - Eg), \quad (1)$$

where A is the absorption coefficient, C is a parameter that associated with the valence and conduction band, $h\nu$ is the absorption energy, and Eg is the band gap. To analysis the tendency of carriers recombination, photoluminescence (PL) spectra were recorded by a fluorescence spectrophotometer (LS-55, American) with an excitation wavelength of 425 nm. To explore the up-conversion performance, luminescence emission spectrum of as-prepared nanoparticles was detected by using a fluorescent spectrometer (FLS980, UK) under 808 nm and 980 nm semiconductor solid laser excitation.

2.3. Photo-electrochemical tests

To research the generation, migration, and recombination of electrons and holes, photocurrent response and electrochemical impedance spectroscopy (EIS) were tested through an electrochemical workstation (Gamry Instrument, INTERFACE 1000) using 0.5 mol/L Na_2SO_4 as the electrolyte. 4 mg photocatalyst was dispersed in 80 μL DI, 20 μL ethanol and 40 μL Nafion and ultrasonically vibrated for 30 min. Then, 50 μL mixed solution was dip-coated onto a 10 × 10 mm indium tin oxide (ITO) glass electrode and dried. The prepared electrode, platinum electrode, and saturation calomel electrode played the roles of the working electrode, counter electrode, and reference electrode, respectively [31–33].

2.4. Photocatalytic performance

Photocatalytic performances of these nanomaterials were investigated by subjecting them to photocatalytic degradation of MO under the irradiation of Xenon lamp. 0.2 g nanoparticles were dispersed in 100 ml suspension with a concentration of 20 mg L^{-1}, stirring for 30 min in the dark to attain absorption equilibrium. All suspension solutions were irradiated with continuous stirring under the Xenon lamp light with an intensity of simulated double solar radiation, which is about 2 kW/m^2. The supernatant was collected every 20 min and its absorbance was analyzed by UV–Vis spectrometer at maximum wavelength (465 nm). The linear relationship between the concentration and absorbance of was significant. And the degree of MO degradation could be determined from Degradation degree = $(A_0\text{-}A_t)/A_0 \times 100$, where A_0 and A_t are MO concentrations of initial and after degradation,

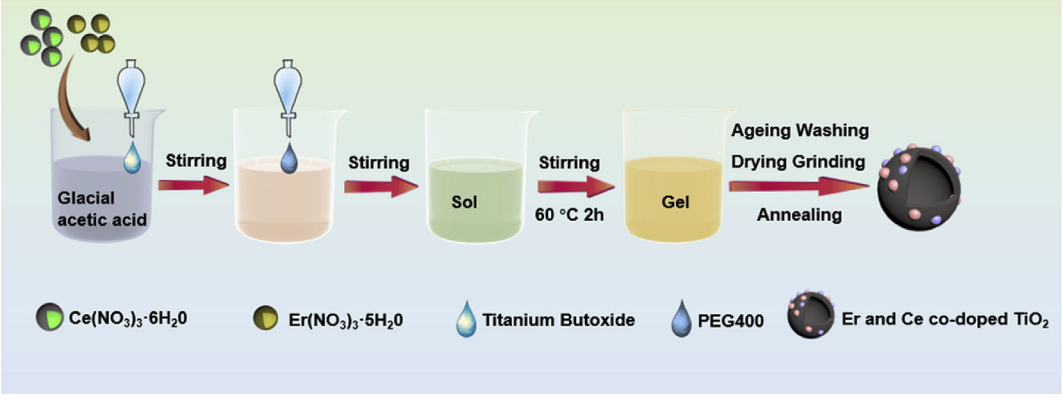

Scheme 1. Typical preparation procedure of TiO_2 NPs with sol-gel method.

respectively [33–35].

2.5. Antimicrobial tests

The antimicrobial performance of photocatalysts was assessed using *Staphylococcus aureus* (*S. aureus*) and *Escherichia coli* (*E. coli*). The nanoparticle with a concentration of 5000 ppm was mixed with bacterial solution which was diluted to 1×10^7 colony-forming units (CFU)/mL in a 96-pore plate. For comparison, an experiment without nanoparticle solutions, instead by same amount of liquid medium was done as control groups. Final solutions were irradiated under the Xenon lamp light for 20 min to simulate natural light, with an intensity of double solar light. After irradiation, 20 μL solution was taken out and diluted. Finally, 20 μL of diluted solution was dropped into agar plate and smeared equably. All agar plates were cultivated at 37 °C for a day [36–38]. The bacterial-killing efficacy can be counted according to the following formula:

Antibacterial ratio (%) = (number of CFUs in control group - number of CFUs in experimental group) / (number of CFUs in control group) × 100%. (2)

3. Results and discussion

3.1. Characterization results of Er doped TiO_2

We first synthesized Er doped TiO_2 with dopant ratio of 0.25 mol%, 0.5 mol%, 0.75 mol% and 1 mol%. Fig. 1 exhibits the UV–vis spectra of the Er–TiO_2 and the pure TiO_2. The UV–vis spectra reveal that the cut-off wavelength doesn't show an evident red shift, which discloses that the band gap has no significant change. However, the absorption of visible region is enhanced along with doping Er, especially in the range of wavelength over 450 nm. In this range, some strong absorption peaks occur at 488 nm, 522 nm, 545 nm, 654 nm, which correspond to electron transition of $4F_{7/2}$, $2H_{11/2}$, $4S_{3/2}$ and $4F_{9/2}$ to ground state, respectively [39]. Among all samples, it is obviously that Er0.5Ti–O shows the best visible light absorption ability. Meanwhile, the Er0.75Ti–O sample presents only tiny difference with Er0.5Ti–O. As the doping content of Er continues to increase, the visible light absorption is decreased gradually with the following trend: Er0.5Ti–O > Er0.75Ti–O > Er1Ti–O > Er0.25Ti–O > TiO_2, which exhibits that the reasonable ratio of Er may be between 0.5 and 0.75 mol%. To evaluate if doped TiO_2 is an efficient up-conversion host material, the up-conversion luminescence properties of these two samples were detected further.

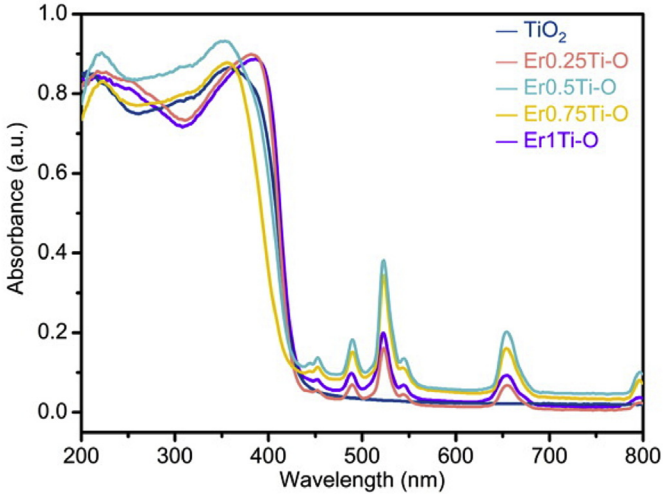

Fig. 1. UV–vis spectra of Er doped TiO_2.

As manifested in Fig. 2(a), the green emission can be observed at 520–570 nm clearly after excited by 808 nm laser, which reveals that TiO_2 is an efficient up-conversion matrix material. When irradiated by 980 nm light source, the green emission decreases but there occurs red emission at 640–690 nm. The synthesized co-doped semiconductors can convert the near-infrared radiation into visible region, which is easier to be utilized by themselves [40,41]. Another discovery is that Er0.75Ti–O sample shows weaker emission than Er0.5Ti–O, which implies that quenching of emission may take place at higher concentration of erbium ions. Therefore, 0.5 mol% is supposed to be the most reasonable ratio and used in our subsequent studies.

As shown in Fig. S1(a), Er0.5Ti–O calcined at 700 °C shows the main characteristic peaks of anatase, namely, the planes (101), (004), (200), (105), (211) and (204) at 2θ = 25.2, 37.8, 48.3, 53.8, 55.0 and 62.7, respectively [42–44]. By contrast, the undoped TiO_2 already transformed into rutile when calcined at 700 °C, and the peaks at 27.4, 36.1, 41.2, 44.1, 54.3 and 56.6° are associated with (110), (101), (111), (210), (211) and (220) of rutile, respectively. The above results suggest that the addition of Er delays the transition of crystal form as reported elsewhere. To get more information of crystal form, we further investigate the XRD spectra of Er0.5Ti–O annealed at 800 °C and 900 °C. When the annealing temperature is 800 °C, there exist both rutile and anatase. When the temperature is rose to 900 °C, all anatase has been transformed into rutile thoroughly, as shown in Fig. S1(b). It has been reported that the photocatalytic properties of mixed crystal TiO_2 NPs are much better than any single crystal [23,45]. In order to get mixed crystal, 800 °C is selected as calcination temperature for further investigation.

3.2. Characterization results of Er–Ce co-doped TiO_2

The XRD spectra of the Er–Ce co-doped samples are shown in Fig. 3(a), from which we can find that all co-doped TiO_2 NPs are mixed crystal as expected. With the increasing of annealing temperature, the ratio of rutile is lessened, indicating that the transition crystal form is delayed due to the addition of Ce. The inhibition by both dopants may be related to formation of Ti–O–Er or Ti–O–Ce bonds [46]. As revealed in Fig. 3(b), UV–vis spectra indicate that the responsive toward visible light irradiation is obviously enhanced after the addition of Ce. Er0.5-Ce0.2Ti–O exhibits the strongest visible light absorption among all the samples. Hence, it is believed that there is an optimum doping dosage of Ce, similar with Er, which may be about 0.2 mol%. When the concentration is lower than the optimum amount, effective separations of electrons and holes are not achieved. Once the dopant ratio is higher than the optimal concentration, surface barrier becomes higher and space charge regions get narrower, leading to the reduction of catalytic efficiency [47]. Furthermore, compared with the untreated TiO_2, the absorption edge of co-doped samples all show significant red shift (Fig. 3(b)), indicating that band gap of the co-doped catalysts decrease largely, which is related to the incompletely occupied 4f and 5d orbitals of the Ce ions [48]. The characteristic electron orbitals can not only reduce the band energy gap but also inhibit electron–hole recombination rate through providing new energy levels. Consequently, the photocatalytic activities can be enhanced.

Raman spectroscopy is taken to detect the change of surface structural before and after doping. Considering that samples calcined at 800 °C show two crystal forms, which may lead to the peaks of spectrum too complicated to be identified, so we prefer the samples annealed at 700 °C. As revealed in Fig. 3(d), TiO_2 as well as all co-doped TiO_2 show spectra centered in 144 cm^{-1}, 192 cm^{-1}, 400 cm^{-1}, 519 cm^{-1} and 639 cm^{-1}, corresponding to the Raman-active modes of anatase Eg(1), Eg(2), B1g, A1g and Eg(3). Compared with the undoped TiO_2 sample, vibration peaks in doped samples show blue shift, which is induced by some minor structural deformation of TiO_2 [49,50]. Meanwhile, there exist some new Raman bands at 290 cm^{-1}, 340 cm^{-1} and 520 cm^{-1}, which may result from the RE ions located at different

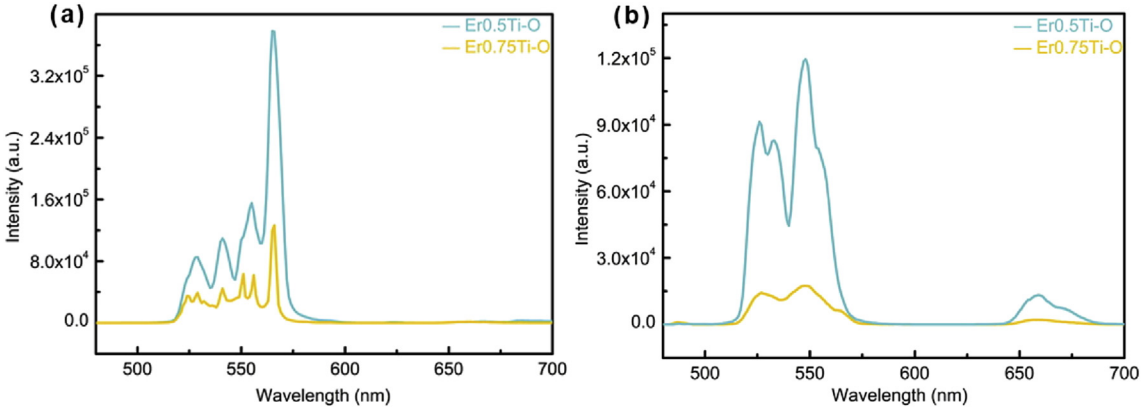

Fig. 2. Up-conversion luminescence spectra for Er0.5Ti–O and Er0.75Ti–O under 880 nm (a) and 980 nm (b) excitation.

sites within the TiO_2 framework [51]. Although there are relatively great differences between radii of Ti ions, Ce ions and Er ions, it has been proposed that there are interstitial channels in anatase crystalline, so that Ce^{3+}/Ce^{4+} and Er^{3+} can gain access to substitute some Ti^{4+} [48].

Fig. 4(a) presents the SEM morphologies of Er0.5Ce0.2Ti–O sample and its EDS composition spectrum is shown in Fig. 4(b). The SEM image shows that the Er0.5Ce0.2Ti–O we prepared are spherical particles with uneven radius, which may be caused by slight aggregation. And the EDS composition spectrum discloses the existence of O, Ti, C, Ce and Er element on the surface. TEM image of Er0.5Ce0.2Ti–O is shown in Fig. 4(c), from which polyhedral structures mainly constituted of hexagonal and rhombus can be seen, with an average size of 30 nm. The HRTEM image is demonstrated in Fig. 4(d), in which the (112) crystal spacing of anatase and the (110) of rutile is marked. And the SAED pattern shown in Fig. 4(e) exhibits polycrystalline rings corresponding to (101) and (105) planes of anatase and (101) of rutile, which confirm the existence of two crystals, agreeing with the results of XRD spectra.

The surface chemical composition of Er0.5Ce0.2Ti–O investigated by XPS is demonstrated in Fig. S2. From the survey of full scan spectra, O 1s, Ti 2p, and C 1s are detected. The adventitious C 1s peak may be led by the contamination because the samples were exposed to atmosphere. As for Ce and Er, the doping amount is too low to identify their signal peaks in the full scan spectra. The high resolution spectra have been fitted. The binding energy centered in 458.5 eV and 464.2 eV correspond to the 2p3/2 and 2p1/2 core level of Ti^{4+} [33,41]. Fig. 5(c) displays the O 1s spectra with peaks at 529.0 eV, 531.2 eV, and 533.0 eV. The first one is attributed to oxygen lattice, while the peak at 531.2 eV is correlated to surface hydroxyl groups, and the peak at 533.0 eV is associated with surface adsorbed oxygen species [33]. The

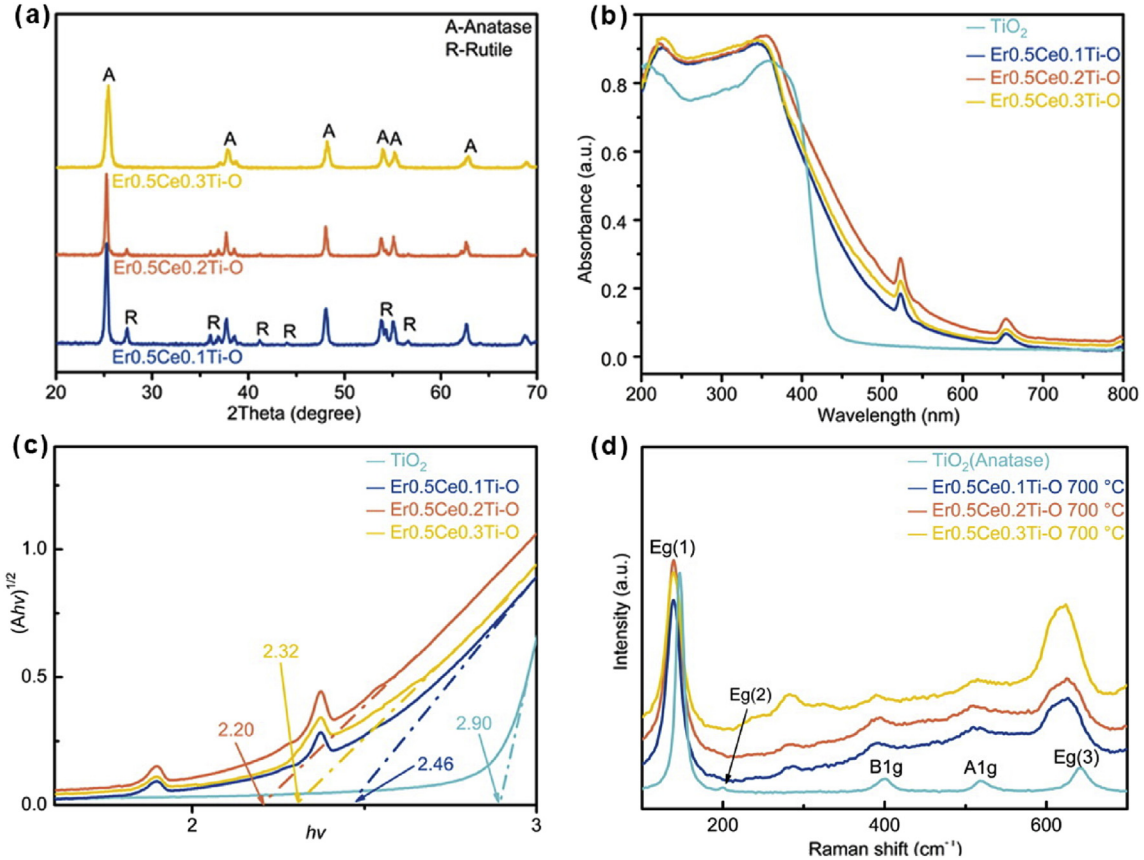

Fig. 3. Characterization of co-doped TiO_2. (a) XRD, (b) UV–vis spectra, (c) band energy gap and (d) Raman spectroscopy.

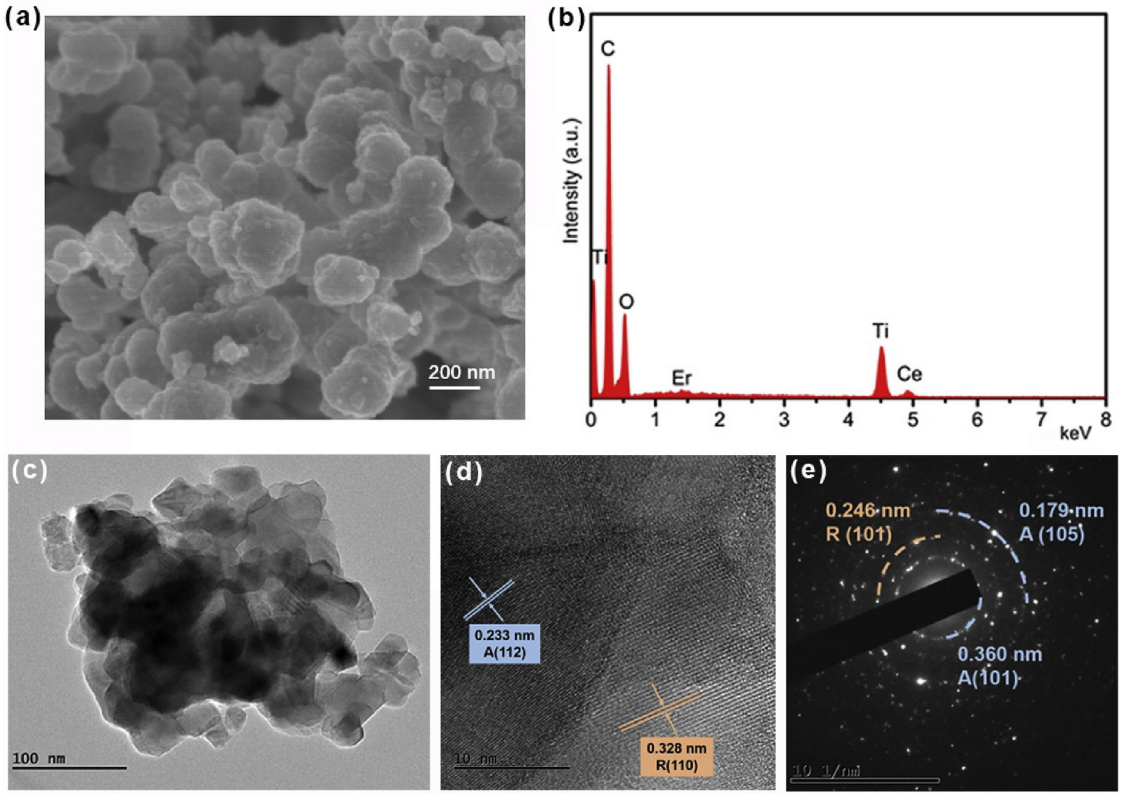

Fig. 4. Characterizations of the Er0.5Ce0.2Ti–O. (a) SEM image, (b) EDS spectrum, (c) TEM image, (d) High-resolution TEM image and (e) selected area electron diffraction (SAED) pattern.

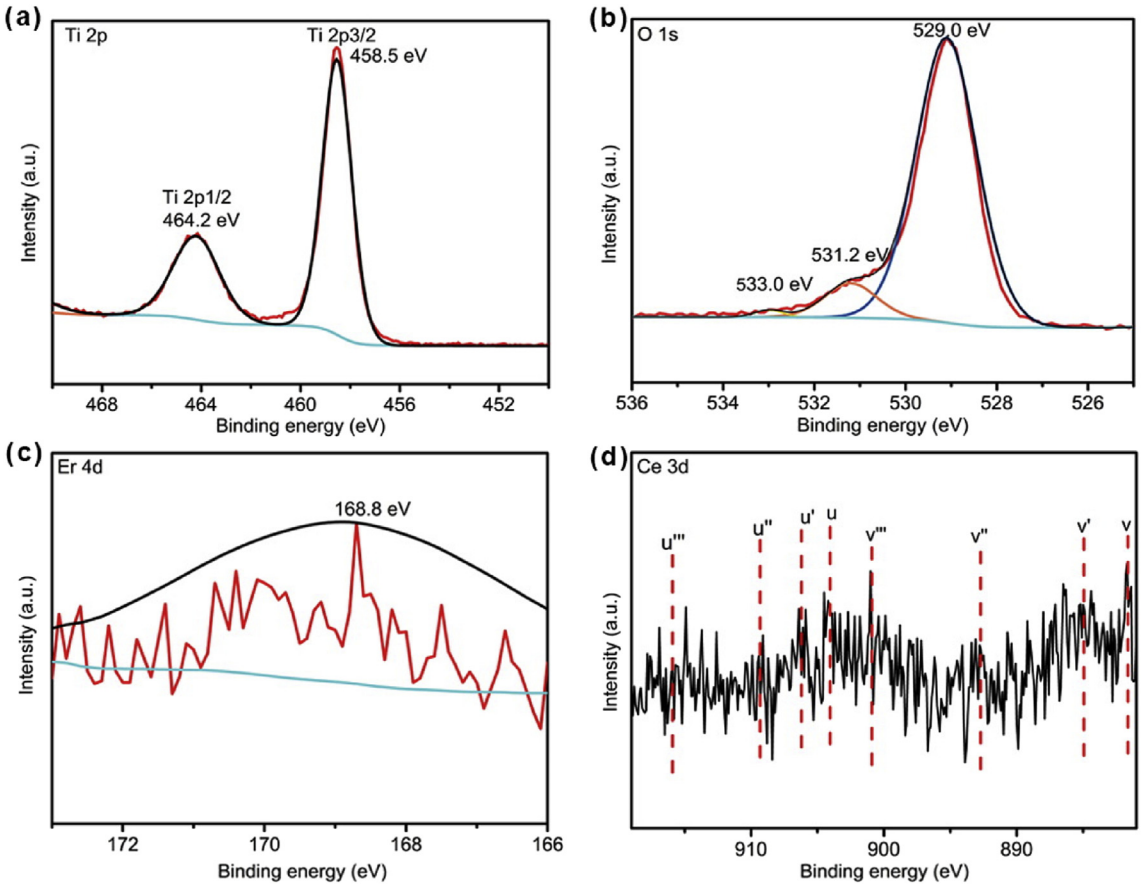

Fig. 5. High-resolution spectra of Ti 2p (a), O 1s (b), Er 4d (c) and Ce 3d (d) for Er0.5Ce0.2Ti–O.

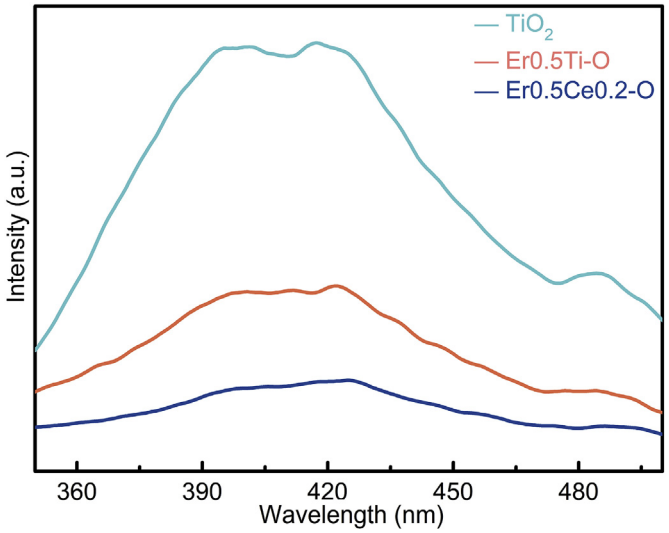

Fig. 6. PL spectra of pure TiO_2, Er0.5Ti–O and Er0.5Ce0.2Ti–O.

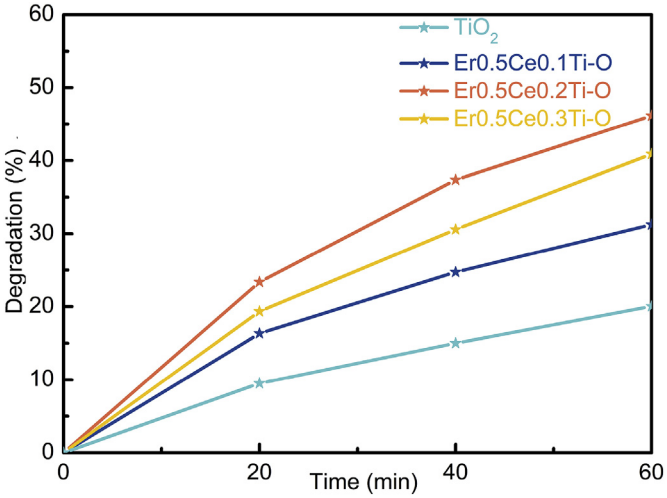

Fig. 8. The degradation rates of MO in the presence of co-doped TiO_2.

peaks located at 168.8 eV corresponds to the Er 4d, which is attributed to Er^{3+} [52]. The XPS peak of cerium is affected by the orbital hybridization of Ce 4f and O 2p, presenting four pairs of spin-orbit splitting bands. The v, v'' and v''' marked in Fig. 5(d) all correspond to Ce IV, confirming the existence of Ce^{4+} state, and u, u'' and u''' owe to O 2p orbital. Meanwhile, the v' and u' denote the existence of Ce^{3+} [42,48,53]. The existence of Ce^{3+}/Ce^{4+} mixture on the surface of photocatalysts can interact with photogenerated holes and electrons, preventing their recombination, leading to a higher catalysis efficiency [48].

It's accepted that the PL intensity is connected with the combination of electrons and holes directly. To be specific, lower PL intensity indicates slower combination rate and longer lifespan of photogenerated carries [33,49]. As shown in Fig. 6, pure TiO_2 exhibits a strong emission peak between 390 nm and 420 nm, caused by the recombination of electron–hole pairs. The intensity of PL spectra deceases obviously after doping Er, which represents a better separation of photogenerated electron-hole. Some researchers have point out that electrons on the valence band (VB) can be excited to some intermediate energy levels by up-conversion emission of Er^{3+}, and then transferred to the conduction band (CB) [46]. Hence, more photogenerated electrons and holes are obtained. And after the presence of Ce ions, the PL intensity continues to become lower, indicating that the electron-hole recombination is inhibited further. We ascribe it to the existence of Ce^{3+}/Ce^{4+} on the surface of TiO_2. To forcefully prove that Ce alone can inhibit the recombination of electron-hole pairs, we processed Ce single-doped sample with 0.2 mol% Ce and measured its PL intensity, which is supplied in Fig. S3. Through the comparison of TiO_2 and Ce0.2Ti–O, we can draw a conclusion that the addition of Ce can suppress the combination of generated carriers.

3.3. Photo-electrochemistry tests

Both EIS and photocurrent response are relatively powerful methods for characterizing photo-electrical properties of photocatalysts. It can be clearly seen from Fig. 7(a) that the diameter of Nyquist semicircle of TiO_2 is significantly narrowed after doping, suggesting that the carriers transfer resistance is effectively bring and the surface reaction is boosted. It is widely accepted that the photocurrent intensity is decided by the separation efficiency of photogenerated carriers. As shown in Fig. 7 (b), the composite has weak current response in the dark and exhibits a steady current when exposed to Xenon lamp light. Moreover, the photo current is enhanced after doping, indicating that the separation and transition efficiency of carriers can be enhanced visibly along with doping modification.

3.4. Photocatalytic performance

As shown in Fig. 8, pure TiO_2 photocatalysts can degrade 20.04% of MB in 60 min. The degrading rate is improved when using co-doped

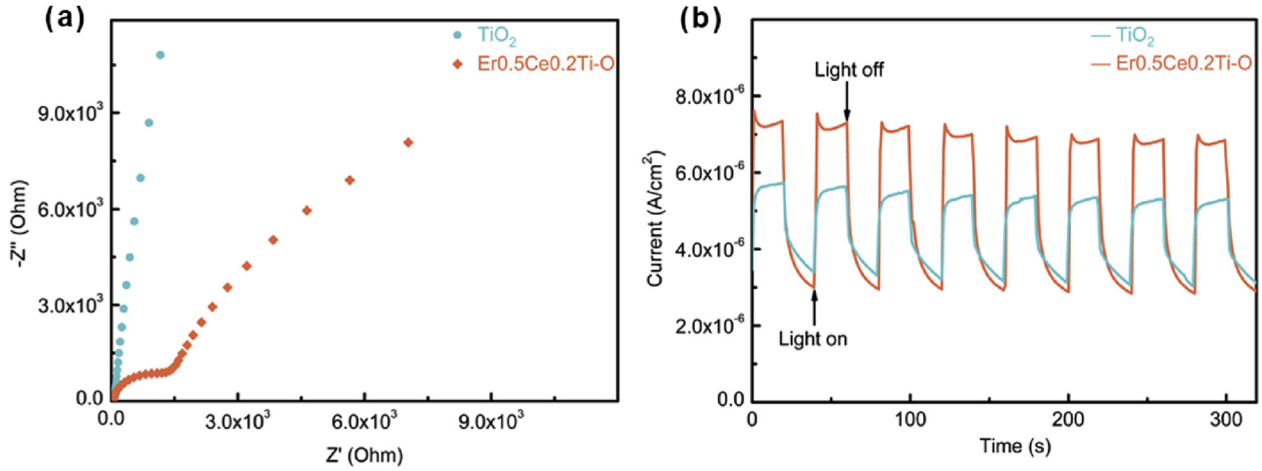

Fig. 7. EIS plots (a) and the photocurrent spectra (b) of pure TiO_2 and modified TiO_2.

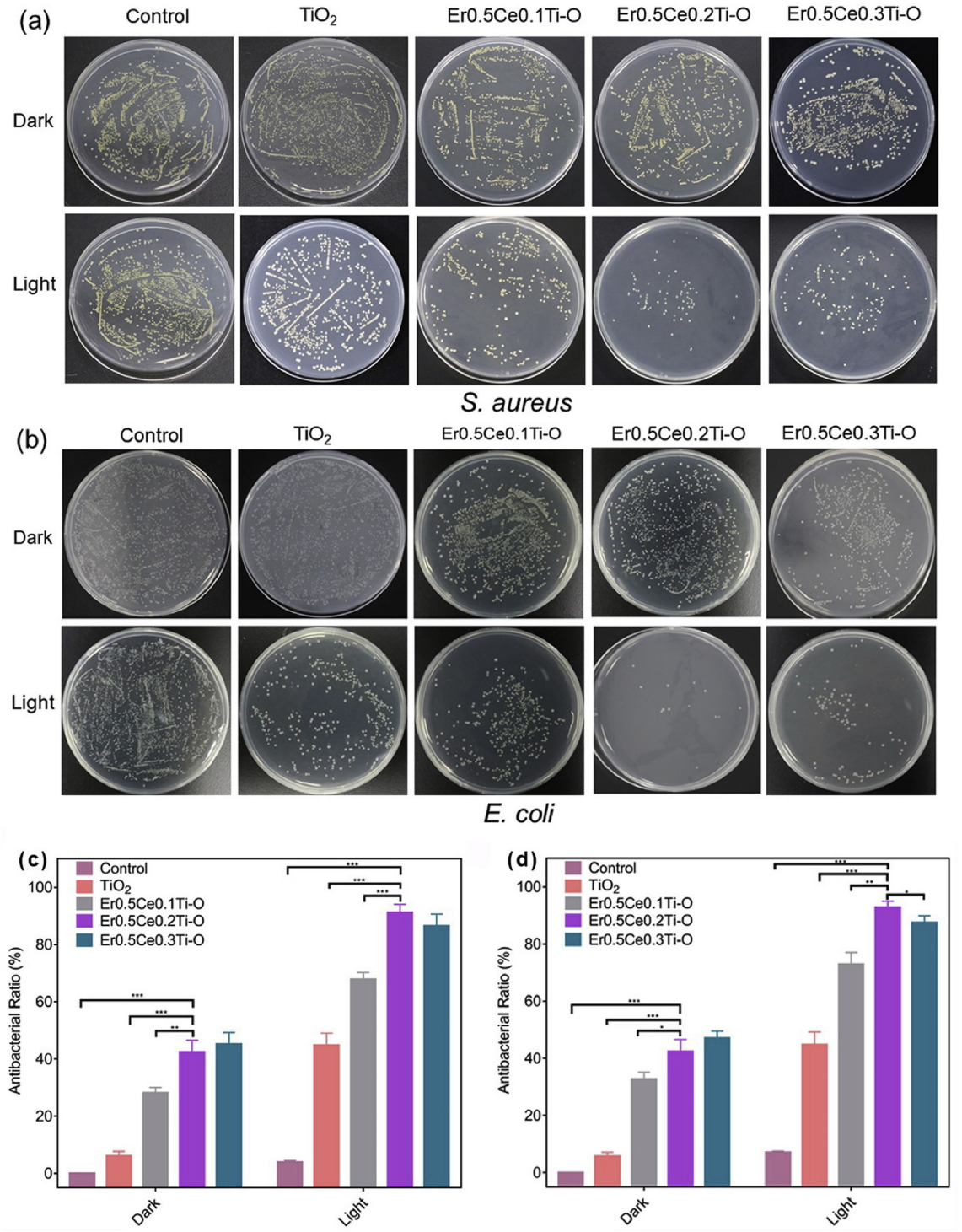

Fig. 9. The formed viable colony units of *S. aureus* (a) and *E. coli* (b) after treated with samples in the dark for 20 min or under simulated sunlight for 20 min and the corresponding abilities of the samples in killing *S. aureus* (c) and *E. coli* (d). The experiment was performed in triplicate and independently. (n = 3, mean ± SD).

TiO_2, and the Er0.5Ce0.2Ti–O composite exhibits the best photodegradation activity, which could degrade 46.13% MO within 60 min. The addition of Er element successfully turns the near-infrared radiation of the sunlight into visible light and Ce ions can effectively extend the range of spectral response. Meanwhile, both RE ions can improve the separation efficiency and migration rate of the interface carriers, restraining the recombination of electrons and holes. Thus, the photocatalytic activity of co-doped TiO_2 is enhanced obviously.

3.5. Antimicrobial performance

In vitro *E. coli* and *S. aureus* antibacterial activities of different samples are given in Fig. 9. It can be seen from Fig. 9 that bacterial colonies on TiO_2 are slightly less than that on the control group after visible light irradiation of 20 min with an intensity of double solar light, and the bacterial colonies on doped TiO_2 decrease massively. Among all co-doped groups, the Er0.5Ce0.2Ti–O shows the best antibacterial efficacy, whose antibacterial ratios toward *E. coli* and *S. aureus* are 92.8%

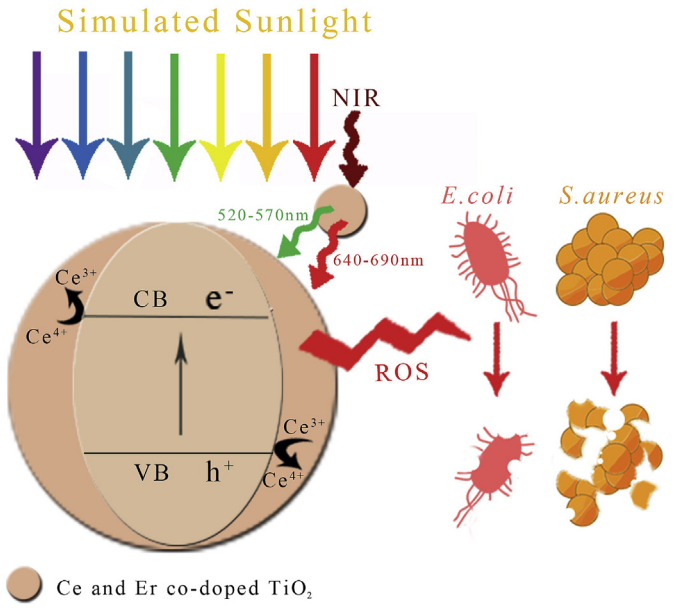

Fig. 10. Schematic illustration of the mechanism of enhanced photocatalytic disinfection of Ce and Er co-doped TiO_2.

and 91.23%, respectively, compared to 44.79% and 44.85% of undoped TiO_2. The results of antibacterial activities mainly agree with photocatalytic results. That is to say that the better photocatalytic performance means more ROS generated during visible light irradiation, thus providing better antibacterial property [54]. Obviously, the co-doped nanoparticles exhibit antibacterial effects without external activation as well and the antibacterial performance is intensified with the increase of Ce. Therefore, we consider that the antibacterial performance in the absence of irradiation arises from Ce ions. In fact, previous studies have put forward that Ce ions have antibacterial effects based on the reaction with cell walls and interference with bacterial cellular respiration [55].

The mechanism of the enhanced photocatalytic disinfection is schematically illustrated in Fig. 10. After doping modification by Ce, the energy gap of TiO_2 is decreased, which means that it can harvest not only pure UV but also visible light and generate more ROS when exposing to solar sunlight. Meanwhile, the addition of Er can turn the near-infrared region into visible range, which is easier to be absorbed by synthesized TiO_2. What's more, both Ce and Er ions can inhibit the recombination of photogenerated charge carriers thanks to the incompletely occupied 4f and 5d electron orbitals, thus enhancing the photocatalytic activity effectively. In conclusion, the dual elements doped TiO_2 can be driven by solar sunlight to display outstanding visible light photocatalytic performance for rapid sterilization eco-friendly.

4. Conclusions

In this work, the dual elements doped TiO_2 NPs were synthesized using sol–gel method, which displayed superior visible light photocatalytic performance than the untreated ones. The doped Er can convert the near-infrared radiation of the solar spectrum into visible region, improving the visible light absorption of synthesized TiO_2 NPs while the addition of Ce can broaden absorption spectra of TiO_2 NPs and decrease their energy gap. In addition, the two kinds of RE ions can hinder the recombination of electrons and holes, which can enhance the photocatalytic properties effectively. The optimum dosage of Er and Ce may approximate to 0.5 mol% and 0.2 mol%, respectively, which can endow the doped TiO_2 calcined at 800 °C with higher antibacterial efficacy of 91.23% and 92.8% against *S. aureus* and *E. coli*, respectively under the visible light irradiation.

CRediT authorship contribution statement

Yawei Ren: Conceptualization, Methodology, Data curation, Writing - original draft. **Yajing Han:** Conceptualization, Methodology, Data curation. **Zhaoyang Li:** Methodology. **Xiangmei Liu:** Conceptualization, Writing - review & editing, Supervision, Project administration. **Shengli Zhu:** Methodology. **Yanqin Liang:** Methodology. **Kelvin Wai Kwok Yeung:** Methodology. **Shuilin Wu:** Conceptualization, Writing - review & editing, Supervision, Project administration.

Declaration of competing interest

The authors declare no conflict of interest.

Acknowledgments

This work is jointly supported by the National Science Fund for Distinguished Young Scholars 51925104, National Natural Science Foundation of China nos. 51871162, 51671081, Natural Science Fund of Hubei Province, 2018CFA064, RGC/NSFC (N_HKU725-1616), Hong Kong ITC (ITS/287/17, GHX/002/14SZ), as well as Health and Medical Research Fund (No. 03142446).

Appendix A. Supplementary data

Supplementary data to this article can be found online at https://doi.org/10.1016/j.bioactmat.2020.02.005.

References

[1] P.A. Smith, M.F.T. Koehler, H.S. Girgis, D. Yan, Y. Chen, Y. Chen, J.J. Crawford, M.R. Durk, R.I. Higuchi, J. Kang, J. Murray, P. Paraselli, S. Park, W. Phung, J.G. Quinn, T.C. Roberts, L. Rougé, J.B. Schwarz, E. Skippington, J. Wai, M. Xu, Z. Yu, H. Zhang, M.W. Tan, C.E. Heise, Optimized arylomycins are a new class of Gram-negative antibiotics, Nature 561 (7722) (2018) 189–194.

[2] J. Li, X. Liu, L. Tan, Z. Cui, X. Yang, Y. Liang, Z. Li, S. Zhu, Y. Zheng, K.W.K. Yeung, X. Wang, S. Wu, Zinc-doped Prussian blue enhances photothermal clearance of Staphylococcus aureus and promotes tissue repair in infected wounds, Nat. Commun. 10 (1) (2019) 4490.

[3] L. Tan, J. Li, X. Liu, Z. Cui, X. Yang, S. Zhu, Z. Li, X. Yuan, Y. Zheng, K.W.K. Yeung, H. Pan, X. Wang, S. Wu, Rapid biofilm eradication on bone implants using red Phosphorus and near-infrared light, Adv. Mater. 30 (31) (2018) 1801808.

[4] M. Hamad, F. Al-Marzooq, G. Orive, T.H. Al-Tel, Superbugs but no drugs: steps in averting a post-antibiotic era, Drug Discov. Today 24 (12) (2019) 2225–2228.

[5] R. Laxminarayan, Incentivizing responsible antibiotic use, Science 360 (6387) (2018) 387.

[6] M. Knopp, D.I. Andersson, Predictable phenotypes of antibiotic resistance mutations, mBio 9 (3) (2018) e00770-18.

[7] T. Wei, Q. Yu, H. Chen, Responsive and synergistic antibacterial coatings: fighting against bacteria in a smart and effective way, Adv. Healthc. Mater. 8 (3) (2019) 1801381.

[8] W. Kim, W. Zhu, G.L. Hendricks, D. Van Tyne, A.D. Steele, C.E. Keohane, N. Fricke, A.L. Conery, S. Shen, W. Pan, K. Lee, R. Rajamuthiah, B.B. Fuchs, P.M. Vlahovska, W.M. Wuest, M.S. Gilmore, H. Gao, F.M. Ausubel, E. Mylonakis, A new class of synthetic retinoid antibiotics effective against bacterial persisters, Nature 556 (2018) 103.

[9] G. Liu, S. Zhang, Y. Shi, X. Huang, Y. Tang, P. Chen, W. Si, W. Huang, X. Dong, "Wax-Sealed" theranostic nanoplatform for enhanced afterglow imaging–guided photothermally triggered photodynamic therapy, Adv. Funct. Mater. 28 (42) (2018) 1804317.

[10] M. Li, X. Liu, L. Tan, Z. Cui, X. Yang, Z. Li, Y. Zheng, K.W.K. Yeung, P.K. Chu, S. Wu, Noninvasive rapid bacteria-killing and acceleration of wound healing through photothermal/photodynamic/copper ion synergistic action of a hybrid hydrogel, Biomater. Sci. 6 (8) (2018) 2110–2121.

[11] G. Xiang, C. Ren, Y. Ding, G. Chen, X. Lu, K. Wang, F. Ren, M. Yang, Z. Wang, J. Li, X. An, B. Qian, Y. Leng, Micro/nano-structured TiO_2 surface with dual-functional antibacterial effects for biomedical applications, Bioact. Mater. 4 (2019) 346–357.

[12] B. D'Autréaux, M.B. Toledano, ROS as signalling molecules: mechanisms that generate specificity in ROS homeostasis, Nat. Rev. Mol. Cell Biol. 8 (10) (2007) 813–824.

[13] B. Yang, Y. Chen, J. Shi, Reactive oxygen species (ROS)-based nanomedicine, Chem. Rev. 119 (8) (2019) 4881–4985.

[14] K. Hashimoto, H. Irie, A. Fujishima, TiO_2 Photocatalysis: a historical overview and future prospects, Jpn. J. Appl. Phys., Part 1 44 (12) (2005) 8269–8285.

[15] X. Chen, L. Liu, F. Huang, Black titanium dioxide (TiO_2) nanomaterials, Chem. Soc. Rev. 44 (7) (2015) 1861–1885.

[16] H. Tang, Y. Ren, S. Wei, G. Liu, X. Xu, Preparation of 3D ordered mesoporous anatase TiO2 and their photocatalytic activity, Rare Met. 38 (5) (2019) 453–458.

[17] B. Roose, S. Pathak, U. Steiner, Doping of TiO_2 for sensitized solar cells, Chem. Soc. Rev. 44 (22) (2015) 8326–8349.

[18] L.G. Devi, B.N. Murthy, S.G. Kumar, Photocatalytic activity of V^{5+}, Mo^{6+} and Th^{4+} doped polycrystalline TiO_2 for the degradation of chlorpyrifos under UV/solar light, J. Mol. Catal. Chem. 308 (1) (2009) 174–181.

[19] R. Asahi, T. Morikawa, T. Ohwaki, K. Aoki, Y. Taga, Visible-light photocatalysis in nitrogen-doped titanium oxides, Science 293 (5528) (2001) 269.

[20] V. Kumaravel, S. Mathew, J. Bartlett, S.C. Pillai, Photocatalytic hydrogen production using metal doped TiO_2: a review of recent advances, Appl. Catal., B 244 (2019) 1021–1064.

[21] J.F. Guayaquil-Sosa, B. Serrano-Rosales, P.J. Valadés-Pelayo, H. de Lasa, Photocatalytic hydrogen production using mesoporous TiO_2 doped with Pt, Appl. Catal., B 211 (2017) 337–348.

[22] Y. Zhu, J. Li, C. Dong, J. Ren, Y. Huang, D. Zhao, R. Cai, D. Wei, X. Yang, C. Lv, W. Theis, Y. Bu, W. Han, S. Shen, D. Yang, Red phosphorus decorated and doped TiO_2 nanofibers for efficient photocatalytic hydrogen evolution from pure water, Appl. Catal., B 255 (2019) 117764.

[23] A.M.T. Silva, C.G. Silva, G. Dražić, J.L. Faria, Ce-doped TiO_2 for photocatalytic degradation of chlorophenol, Catal. Today 144 (1) (2009) 13–18.

[24] G. Li, C. Liu, Y. Liu, Different effects of cerium ions doping on properties of anatase and rutile TiO_2, Appl. Surf. Sci. 253 (5) (2006) 2481–2486.

[25] F. Zhang, S.W. Wang, X.J. Liu, L.Q. An, X.Y. Yuan, Upconversion luminescence in Er-doped γ-AlON ceramic phosphors, J. Appl. Phys. 105 (9) (2009) 093542.

[26] F. Auzel, Upconversion and anti-Stokes processes with f and d ions in solids, Chem. Rev. 104 (1) (2004) 139–174.

[27] T. Gu, L. Cheng, F. Gong, J. Xu, X. Li, G. Han, Z. Liu, Upconversion composite nanoparticles for tumor hypoxia modulation and enhanced near-infrared-triggered photodynamic therapy, ACS Appl. Mater. Interfaces 10 (18) (2018) 15494–15503.

[28] C.C. Wang, J.Y. Ying, Sol − gel synthesis and hydrothermal processing of anatase and rutile titania nanocrystals, Chem. Mater. 11 (11) (1999) 3113–3120.

[29] H. Xue, Y. Chen, X. Liu, Q. Qian, Y. Luo, M. Cui, Y. Chen, D.P. Yang, Q. Chen, Visible light-assisted efficient degradation of dye pollutants with biomass-supported TiO_2 hybrids, Mater. Sci. Eng. C 82 (2018) 197–203.

[30] J. Yu, X. Zhao, Q. Zhao, Effect of surface structure on photocatalytic activity of TiO_2 thin films prepared by sol-gel method, Thin Solid Films 379 (1) (2000) 7–14.

[31] W. Xie, L. Liu, W. Cui, W. An, Enhancement of photocatalytic activity under visible light irradiation via the AgI@TCNQ core-shell structure, Materials 12 (10) (2019) 1679.

[32] Y. Zhou, M. Niu, S. Zhu, Y. Liang, Z. Cui, X. Yang, A. Inoue, Preparation and electrocatalytic performance of nanoporous Pd/Sn and Pd/Sn-CuO composite catalysts, Electrochim. Acta 296 (2019) 397–406.

[33] L. Lu, R. Shan, Y. Shi, S. Wang, H. Yuan, A novel TiO_2/biochar composite catalysts for photocatalytic degradation of methyl orange, Chemosphere 222 (2019) 391–398.

[34] L. Wang, Z. Li, J. Chen, Y. Huang, H. Zhang, H. Qiu, Enhanced photocatalytic degradation of methyl orange by porous graphene/ZnO nanocomposite, Environ. Pollut. 249 (2019) 801–811.

[35] J. Yang, J. Du, X. Li, Y. Liu, C. Jiang, W. Qi, K. Zhang, C. Gong, R. Li, M. Luo, H. Peng, Highly hydrophilic TiO_2 nanotubes network by alkaline hydrothermal method for photocatalysis degradation of methyl orange, Nanomaterials 9 (4) (2019) 526.

[36] C. Mao, Y. Xiang, X. Liu, Z. Cui, X. Yang, Z. Li, S. Zhu, Y. Zheng, K.W.K. Yeung, S. Wu, Repeatable photodynamic therapy with triggered signaling pathways of fibroblast cell proliferation and differentiation to promote bacteria-accompanied wound healing, ACS Nano 12 (2) (2018) 1747–1759.

[37] L. Huang, K. Su, Y. Zheng, K.W.K. Yeung, X. Liu, Construction of TiO_2/silane nanofilm on AZ31 magnesium alloy for controlled degradability and enhanced biocompatibility, Rare Met. 38 (6) (2019) 588–600.

[38] B. Huang, L. Tan, X. Liu, J. Li, S. Wu, A facile fabrication of novel stuff with antibacterial property and osteogenic promotion utilizing red phosphorus and near-infrared light, Bioact. Mater. 4 (2019) 17–21.

[39] Q. Shang, H. Yu, X. Kong, H. Wang, X. Wang, Y. Sun, Y. Zhang, Q. Zeng, Green and red up-conversion emissions of Er^{3+}–Yb^{3+} co-doped TiO_2 nanocrystals prepared by sol–gel method, J. Lumin. 128 (7) (2008) 1211–1216.

[40] R. Lahiri, A. Ghosh, S.M.M.D. Dwivedi, S. Chakrabartty, P. Chinnamuthu, A. Mondal, Performance of Erbium-doped TiO_2 thin film grown by physical vapor deposition technique, Appl. Phys. A 123 (9) (2017) 573.

[41] S. Dong, S. Dong, D. Zhou, X. Zhou, D. Ma, Y. Du, Synthesis of Er^{3+}:Al_2O_3-doped and rutile-dominant TiO_2 composite with increased responsive wavelength range and enhanced photocatalytic performance under visible light irradiation, J. Mol. Catal. Chem. 407 (2015) 38–46.

[42] L. Matějová, K. Kočí, M. Reli, L. Čapek, A. Hospodková, P. Peikertová, Z. Matěj, L. Obalová, A. Wach, P. Kuśtrowski, A. Kotarba, Preparation, characterization and photocatalytic properties of cerium doped TiO_2: on the effect of Ce loading on the photocatalytic reduction of carbon dioxide, Appl. Catal., B 152–153 (2014) 172–183.

[43] D.A.H. Hanaor, C.C. Sorrell, Review of the anatase to rutile phase transformation, J. Mater. Sci. 46 (4) (2011) 855–874.

[44] J. Sun, M. Zhang, Z. Wang, H. Chen, Y. Chen, N. Murakami, T. Ohno, Synthesis of anatase TiO_2 with exposed {001} and {101} facets and photocatalytic activity, Rare Met. 38 (4) (2019) 287–291.

[45] H. Zou, L. Wang, H. Tao, Y. Liu, M. Chang, S. Yao, Preparation of SiO_2@TiO_2: Eu^{3+}@TiO_2 core double-shell microspheres for photodegradation of polyacrylamide, RSC Adv. 9 (53) (2019) 30790–30796.

[46] W. Wang, Q. Shang, W. Zheng, H. Yu, X. Feng, Z. Wang, Y. Zhang, G. Li, A Novel near-infrared antibacterial material depending on the upconverting property of Er^{3+}-Yb^{3+}-Fe^{3+} tridoped TiO_2 nanopowder, J. Phys. Chem. C 114 (32) (2010) 13663–13669.

[47] A.W. Xu, Y. Gao, H.Q. Liu, The Preparation, Characterization, and their Photocatalytic activities of rare-earth-doped TiO_2 nanoparticles, J. Catal. 207 (2) (2002) 151–157.

[48] K.A. Ali, A.Z. Abdullah, A.R. Mohamed, Visible light responsive TiO_2 nanoparticles modified using Ce and La for photocatalytic reduction of CO_2: effect of Ce dopant content, Appl. Catal., A 537 (2017) 111–120.

[49] X. Jiang, Y. Zhang, J. Jiang, Y. Rong, Y. Wang, Y. Wu, C. Pan, Characterization of oxygen vacancy associates within hydrogenated TiO_2: a positron annihilation study, J. Phys. Chem. C 116 (42) (2012) 22619–22624.

[50] R. Palomino-Merino, P. Trejo-Garcia, O. Portillo-Moreno, S. Jiménez-Sandoval, S.A. Tomás, O. Zelaya-Angel, R. Lozada-Morales, V.M. Castaño, Red shifts of the Eg (1) Raman mode of nanocrystalline TiO_2: Er monoliths grown by sol–gel process, Opt. Mater. 46 (2015) 345–349.

[51] L.J. Hardwick, M. Holzapfel, P. Novák, L. Dupont, E. Baudrin, Electrochemical lithium insertion into anatase-type TiO_2: an in situ Raman microscopy investigation, Electrochim. Acta 52 (17) (2007) 5357–5367.

[52] L. Song, N. Zhao, F.J. Xu, Hydroxyl-rich polycation brushed multifunctional rare-earth-gold core–shell nanorods for versatile therapy platforms, Adv. Funct. Mater. 27 (32) (2017) 1701255.

[53] E. Paparazzo, On the curve-fitting of XPS Ce(3d) spectra of cerium oxides, Mater. Res. Bull. 46 (2) (2011) 323–326.

[54] Y. Zhang, X. Liu, Z. Li, S. Zhu, X. Yuan, Z. Cui, X. Yang, P.K. Chu, S. Wu, Nano Ag/ZnO-incorporated hydroxyapatite composite coatings: highly effective infection prevention and excellent osteointegration, ACS Appl. Mater. Interfaces 10 (1) (2018) 1266–1277.

[55] P. Bellio, C. Luzi, A. Mancini, S. Cracchiolo, M. Passacantando, L. Di Pietro, M. Perilli, G. Amicosante, S. Santucci, G. Celenza, Cerium oxide nanoparticles as potential antibiotic adjuvant. Effects of CeO_2 nanoparticles on bacterial outer membrane permeability, Biochim. Biophys. Acta 1860 (11) (2018) 2428–2435.